Supporting Information

The 3d-4f electron transition of CoS_2/CeO_2 heterojunction for efficient oxygen evolution

Yaqin Chen,[a#] Yuchao Zhang,[a#] Hui Xue,[*a] Jing Sun,[a] Niankun Guo,[a] Tianshan Song,[a] Jiawen Sun,[a] Yi-Ru Hao,[a] and Qin Wang[*a]

[a] College of Chemistry and Chemical Engineering, Inner Mongolia University, Hohhot 010021 (PR China)

Corresponding authors: E-mail: qinwang@imu.edu.cn (Q. Wang)

[#] These authors contributed equally to this work.

1. Material Synthesis

Chemicals

The cobalt nitrate ($Co(NO_3)_2 \cdot 6H_2O$, AR), cerium nitrate ($Ce(NO_3)_3 \cdot 6H_2O$, AR), urea ($CO(NH_2)_2$, AR), ammonium fluoride (NH_4F, AR) and sulfur powder were purchased from Tianjin Fengchuan Chemical Reagent Factory. The Ni Foam was purchased from Taiyuan LZY Technology Co., Ltd. The potassium hydroxide (KOH, 95%) and ethanol (CH_3CH_2OH, 95%) were purchased from Aladdin. All the chemicals were used without being purified.

Synthesis of CeCo-precursor

Before the hydrothermal treatment, the nickel foam (NF) was sectioned into small

pieces measuring 2×3 cm^2 and subjected to a cleaning process involving 3 M HCl, acetone, ethanol, and deionized water for 15 minutes. A light pink solution was prepared by dissolving 1.0 mmol of $Co(NO_3)_2\cdot6H_2O$, 0.5 mmol of $Ce(NO_3)_3\cdot6H_2O$, 0.3 g of urea, and 0.18 g of NH_4F in 20 mL deionized water, followed by stirring at room temperature for 30 minutes. Subsequently, the solution was transferred into a Teflon-lined autoclave, and the treated NF into the above solution, heated at 140 °C for 8 hours. After cooling to room temperature, the precursor was extracted and washed three times with deionized water and ethanol before being dried overnight at 60 °C.

Synthesis of Co_3O_4/CeO_2

The CeCo-precursor was subjected to oxidation in an air atmosphere within a tube furnace, which was heated to 350 °C and maintained for a duration of 2 hours, resulting in the production of the Co_3O_4/CeO_2 catalyst.

Synthesis of CoS_2/CeO_2

The chemical vapor deposition method was used for vulcanization. Specifically, Co_3O_4/CeO_2 was placed near the outlet end of the tube furnace, and sulfur powder was placed near the inlet end, and heated to 350 °C under a nitrogen atmosphere for 2 hours. Subsequently, the CoS_2/CeO_2 catalyst was successfully synthesized upon cooling to room temperature.

Synthesis of CoS_2

The synthesis of the CoS_2 catalyst on NF was similar to that of the CoS_2/CeO_2 catalyst, with the exception that $Ce(NO_3)_3\cdot6H_2O$ was not added during the hydrothermal step.

Synthesis of CeO_2

The synthesis CeO_2 catalyst on NF was similar to that of the CoS_2/CeO_2 catalyst, with the exception that $Co(NO_3)_3 \cdot 6H_2O$ and NH_4F were not added during the hydrothermal step.

2. Material Characterization

X-ray diffraction (XRD) profiles (2θ, 5-80°) were acquired on a PuXi XD3 diffractometer with Cu Kα (λ = 0.15406 nm). X-ray photoelectron spectra (XPS) were corrected using the C 1s line at 284.8 eV and measured using an ESCA-LAB 250 X-ray electron spectrometer equipped with Al Kα radiation. The scanning electron microscopy (SEM) images were performed on Field Emission Scanning Electron Microscopy (FESEM, JEOL JSM-7600F). Transmission electron microscopy (TEM) and high-resolution transmission electron microscopy (HRTEM) images were recorded on a JEM-2100F transmission electron microscope system. Electron paramagnetic resonance (EPR) tests were performed using the JES FA200 electron paramagnetic resonance spectrometer. The Raman spectra were analyzed by a Renishaw inVia Raman spectrometer with a 532 nm laser as excitation source.

3. Electrochemical Test

All electrochemical measurements were performed on a CHI760e (Shanghai, China) electrochemical workstation using a standard three-electrode system. The nickel foam with the catalyst was used as the working electrode (area of ~1×0.5 cm²), the saturated calomel electrode as the reference electrode, and the carbon rod as the counter electrode, respectively. The linear sweep voltammetry (LSV) curves were performed in the range of 0 to 1 V (vs. SCE) for OER and UOR in an alkaline solution at the scan

rate of 2 mV s^{-1}. The double-layer capacitance (C_{dl}) of the catalysts at different scanning rates was measured by cyclic voltammetry (CV) in the non-Faraday region. Electrochemical impedance spectroscopy (EIS) was performed at 0.45 V and in alkaline solution. The potentiostatic test curves (i-t) were measured with a constant potential to investigate its stability. The Faraday efficiency is measured by the drainage method. The theoretical O$_2$ precipitation is calculated by Faraday's law and I-t curve, and compared with the actual oxygen production produced in the test process. The diffuse reflection absorption curve is obtained by using a UV-VIS spectrometer (UV-3600i Plus), and the test band is 200-800 nm.

4. DFT Methods

We have employed the first principles[1] to perform all spin-polarization density functional theory (DFT) calculations within the generalized gradient approximation (GGA) using the Perdew-Burke-Ernzerhof (PBE) [3] formulation. The cut-off energy for the plane wave basis is set to 400 eV and a 4×4×1 K-point mesh is employed. The Hubbard-type U correction for the strong-correlation 3d and 4f electrons of Co and Ce are 3.4 and 2.3 eV, respectively (GGA+U). [4] Relativistic spin-orbit coupling (SOC) was included in the density of states calculations. All the structures were fully relaxed (atomic position) up to 10^{-5} eV/Å force minimization and max force of 0.01 eV/ Å.

We have chosen the projected augmented wave (PAW) [5,6] potentials to describe the ionic cores and take valence electrons into account using a plane wave basis set with a kinetic energy cutoff of 520 eV. The GGA+U method was adopted in our calculations. The value of the effective Hubbard U was set as 4.814 eV for Ce Partial occupancies

of the Kohn−Sham orbitals were allowed using the Gaussian smearing method and a width of 0.05 eV. The electronic energy was considered self-consistent when the energy change was smaller than 10^{-5} eV. A geometry optimization was considered convergent when the energy change was smaller than 0.05 eV·Å^{-1}. The Brillouin zone integration is performed using 2×2×1 Monkhorst-Pack k-point sampling for a structure. Finally, the adsorption energies (E_{ads}) were calculated as $E_{ads}= E_{ad/sub} -E_{ad} -E_{sub}$, where $E_{ad/sub}$, E_{ad}, and E_{sub} are the total energies of the optimized adsorbate/substrate system, the adsorbate in the structure, and the clean substrate, respectively. The free energy was calculated using the equation:

$G=E_{ads}+ZPE-TS$

where G, Eads, ZPE, and TS are the free energy, total energy from DFT calculations, zero-point energy, and entropic contributions, respectively, where T is set to 300 K. [7]
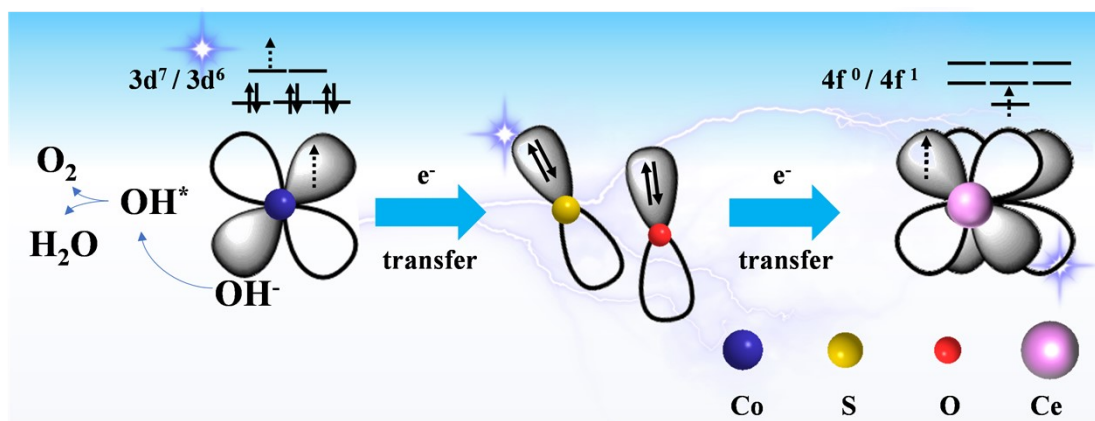
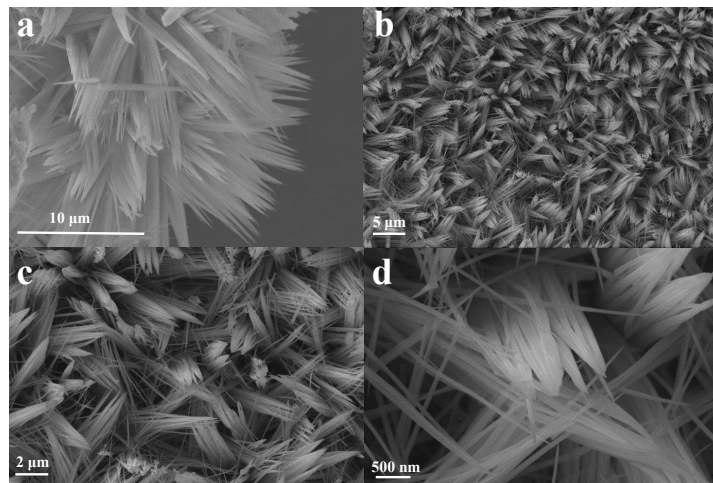**Fig. S1** Prediction of interfacial charge transfer between CoS_2 and CeO_2 based on track coupling engineering.

Fig. S2 SEM images of the (a) CeCo-precursor and (b-d) Co_3O_4/CeO_2 catalyst.

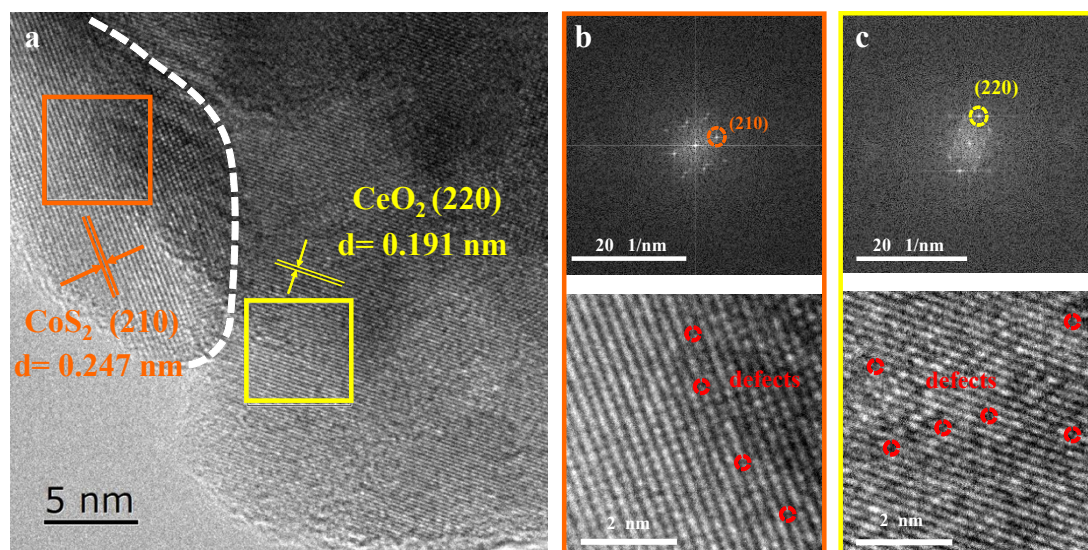**Fig. S3** (a) HRTEM image of the Co_3O_4/CeO_2 catalyst and (b, c) FFT and inverse FFT images corresponding to different color regions, respectively.
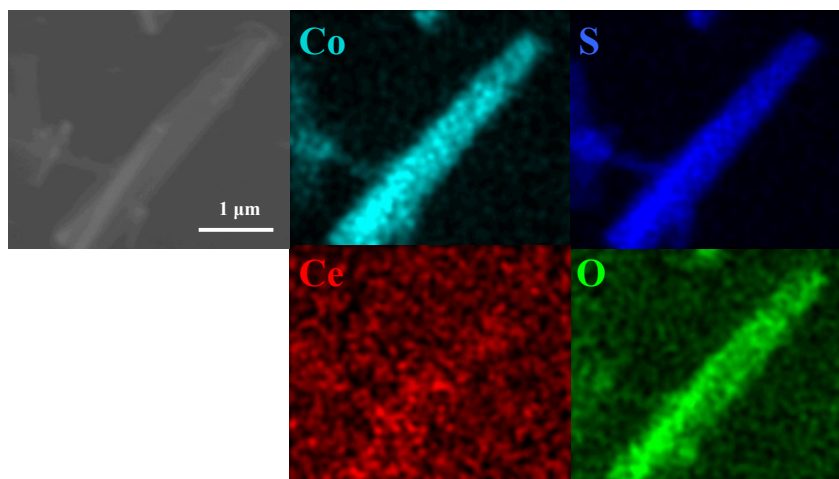
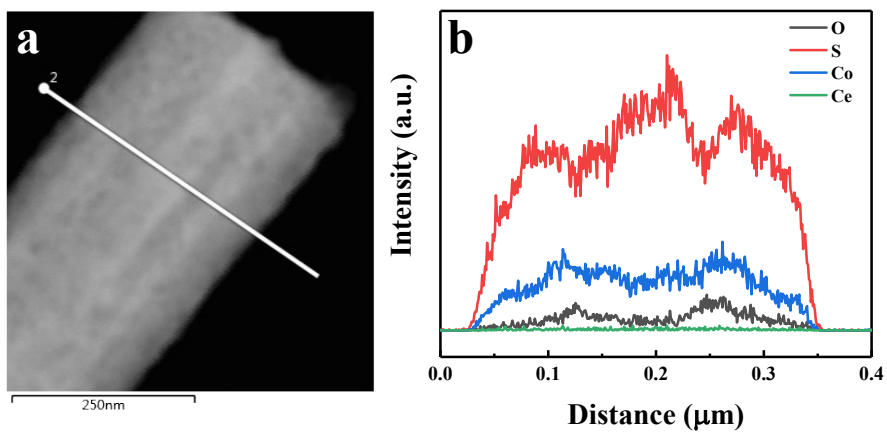**Fig. S4** SEM-elemental mapping of CoS_2/CeO_2 catalyst.

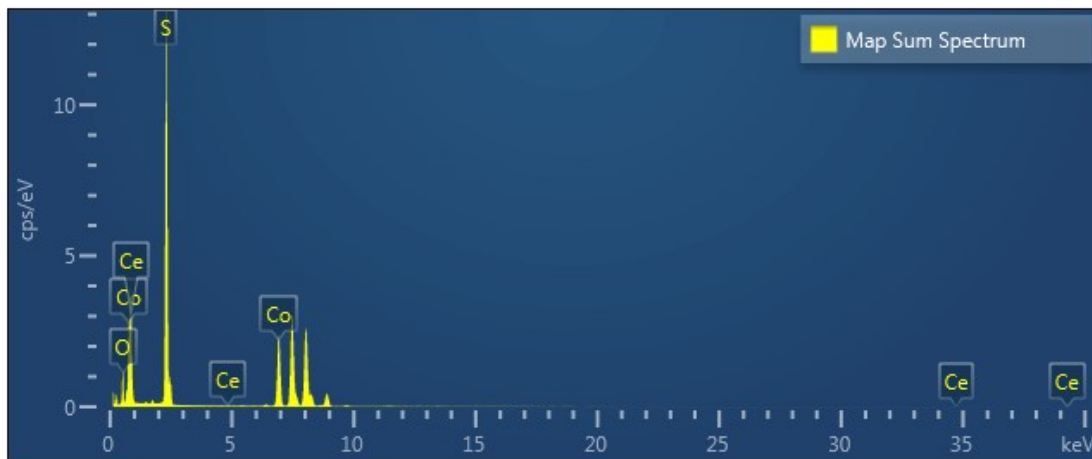**Fig. S5** Line scanning profiles of the CoS$_2$/CeO$_2$ catalyst.

Fig. S6 EDX spectra of the CoS_2/CeO_2 catalysts.

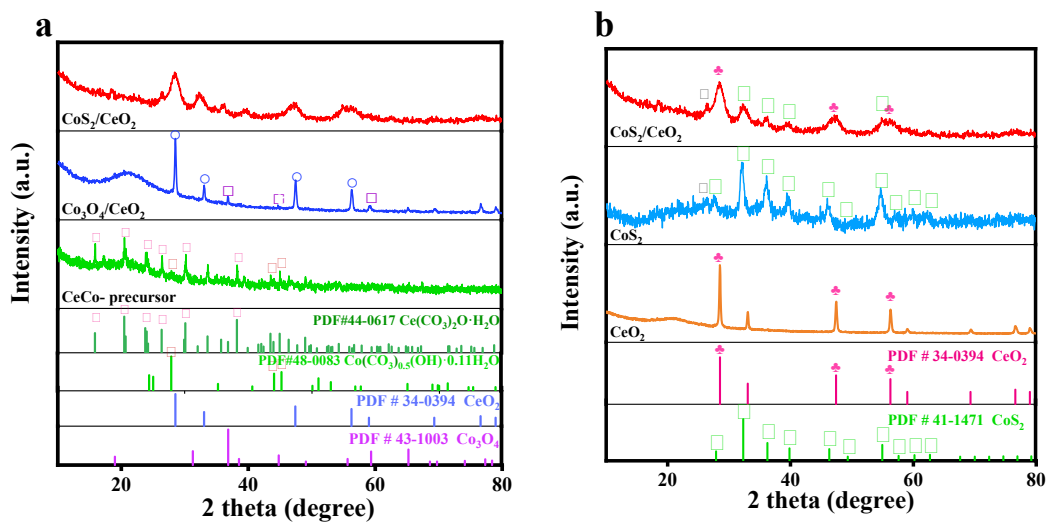**Fig. S7** XRD patterns of (a) the CeCo-precursor, Co_3O_4/CeO_2, and CoS_2/CeO_2 powder catalysts, (b) the CeO_2, CoS_2 and CoS_2/CeO_2 powder catalysts.
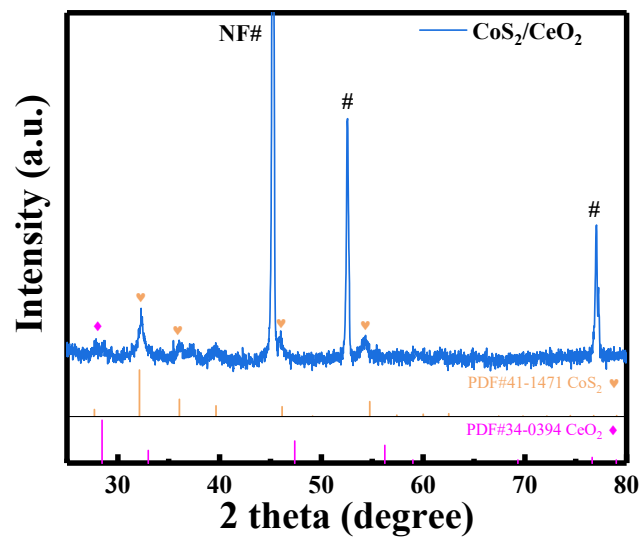
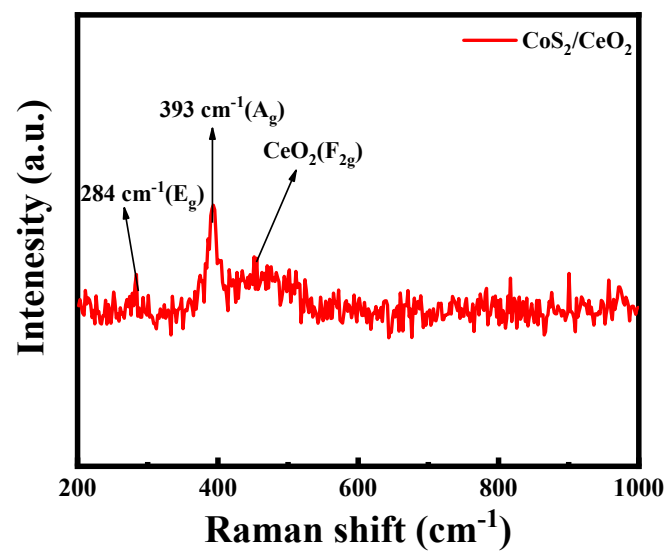**Fig. S8** XRD pattern of CoS_2/CeO_2 catalyst grown on nickel foam.

Fig. S9 Raman spectra of the CoS$_2$/CeO$_2$ catalyst.
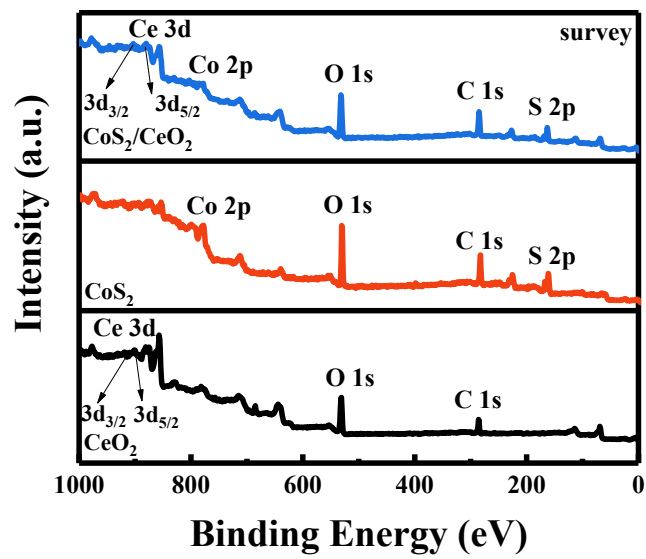
Fig. S10 XPS survey of CeO$_2$, CoS$_2$, and CoS$_2$/CeO$_2$ catalysts.
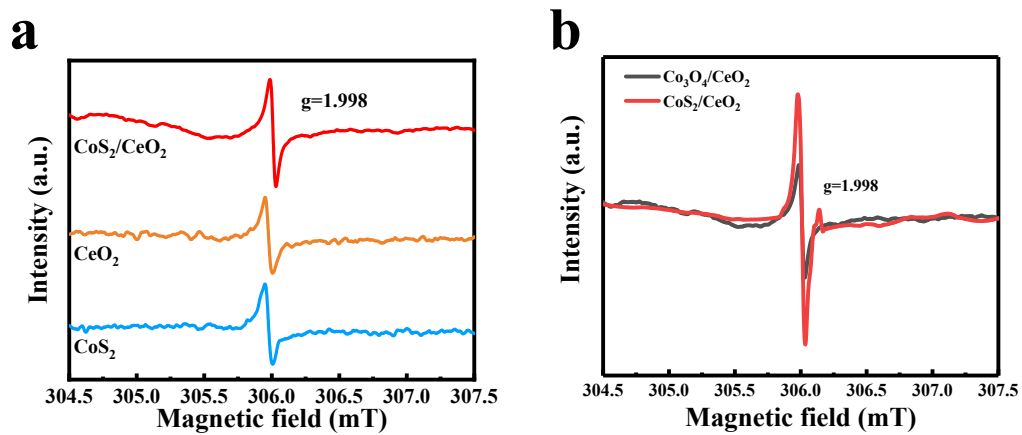
Fig. S11 (a) The EPR spectra of CoS_2, CeO_2 and CoS_2/CeO_2 catalysts, and (b) The EPR spectra of Co_3O_4/CeO_2 and CoS_2/CeO_2 catalysts.
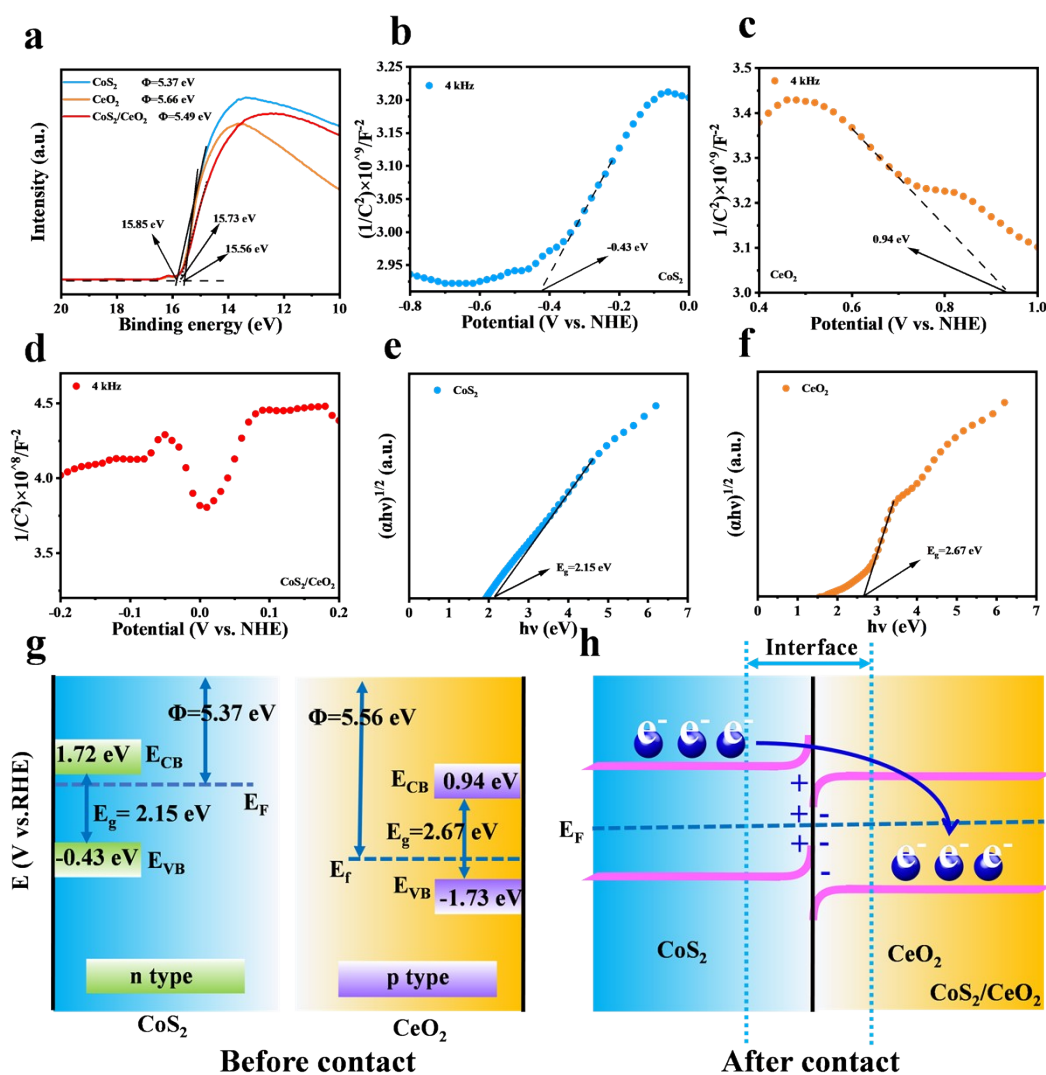
Figure S12. (a) UPS spectra of the CoS_2/CeO_2, CoS_2 and CeO_2 catalysts. The secondary electron cutoff is obtained. Mott-Schottky plots: (b) CoS_2; (c) CeO_2; (d) CoS_2/CeO_2. UV-VIS spectra test of (e) CoS_2 and (f) CeO_2. (g) Energy band structure alignments of CoS_2 and CeO_2 (CB = conduction band, VB = valence band, E_F = Fermi level, E_g = band gap, and Φ = work function). (h) Schematic of interface electronic structure in CoS_2/CeO_2.

We investigated the electron transfer capability of the catalysts through the UPS test (Fig. S12a). The E_{cuff} of the CoS_2 and CeO_2 are 15.85 eV and 15.56 eV, respectively. And the work function (Φ) values are 5.37 eV and 5.56 eV (calculated by the formula $\Phi = h\nu - E_{Cutoff} + E_F$). As can be seen from Mott–Schottky plots in Fig. S12b-d, the slope of CoS_2 is positive, indicating that it is an n-type semiconductor

(E_{VB}= -0.43 eV); on the contrary, the slope of CeO_2 is negative, indicating that it is a p-type semiconductor with E_{CB} = 0.94 eV; and the Mott-Schottky plots of CoS_2/CeO_2 catalyst shows a standard p-n heterojunction semiconductor. Fig. S12e and S12f show the UV-Vis spectra of CoS_2 and CeO_2, from which we can infer that the bandgaps E_g are 2.15 and 2.67 eV, respectively. In order to study the charge transfer between CoS_2 and CeO_2, band maps before and after contact are provided (Fig. S12g and S12h). This proves that the Mott-Schottky barrier will be generated between the two phases. On the one hand, electrons will spontaneously transfer from CoS_2 to CeO_2 with a lower Fermi level; on the other hand, with the progress of electron migration, CeO_2 will be negatively charged and the free electrons near the CoS_2 interface will be depleted, and positively charged, thus forming an internal electric field to achieve electron redistribution until the Fermi levels of both sides reach equilibrium. Therefore, the heterogeneous interface formed by the CoS_2/CeO_2 catalyst can effectively promote electron transport and enhance electrical conductivity.
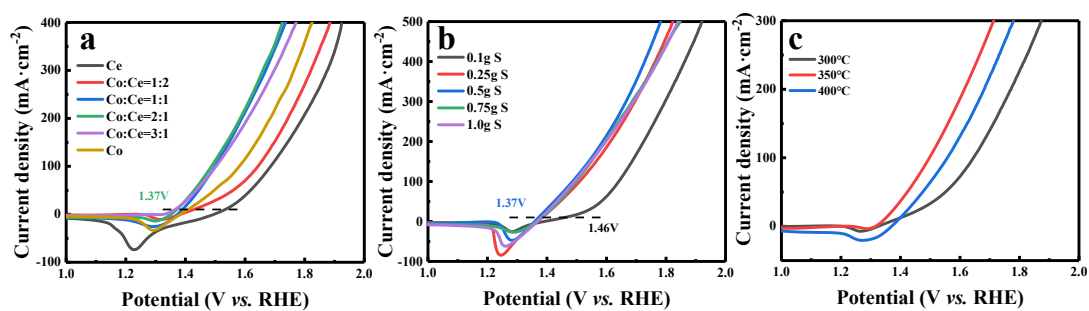
Fig. S13 OER polarization curves of the different catalysts with (a) different molar ratios of Co and Ce, (b) different amounts of sublimed sulfur powder, and (c) different sulfuration temperatures.
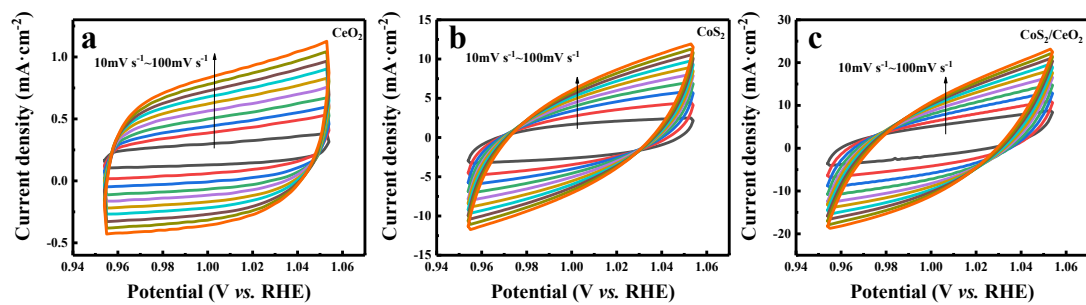
Fig. S14 CV curves at scan rates from 10 mV·s^{-1} to 100 mV·s^{-1} for various catalysts: (a) CeO$_2$, (b) CoS$_2$, (c) CoS$_2$/CeO$_2$ in 1.0 M KOH solution.
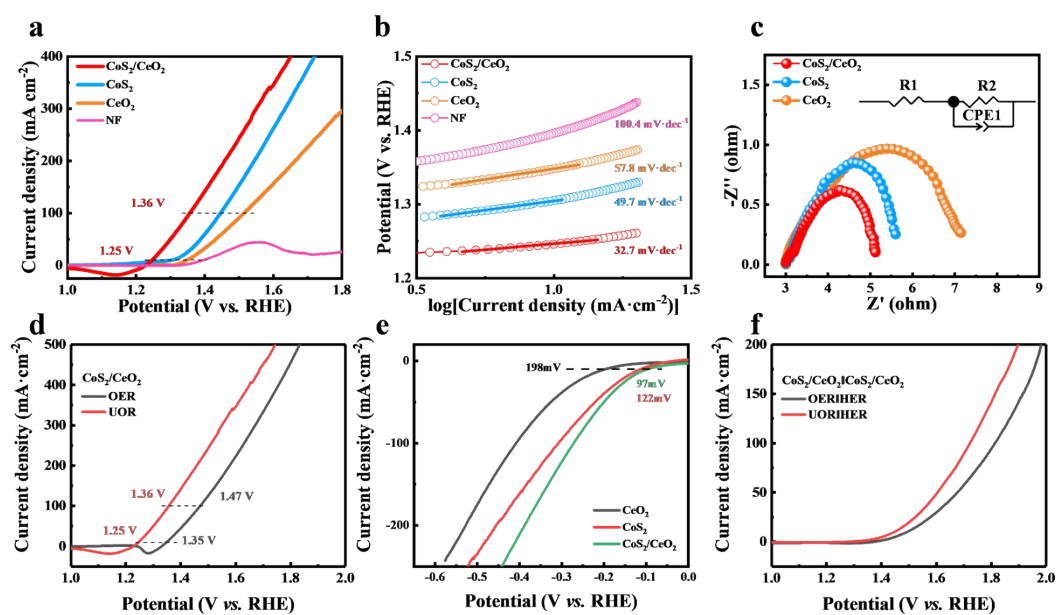
Fig. S15 (a) UOR polarization curves in 1.0 M KOH and 0.5 M urea, (b) UOR Tafel slopes, (c) UOR Nyquist plots, (d) OER and UOR polarization curves, (e) HER polarization curves, and (f) overall water splitting and urea hybrid overall water splitting polarization curves.

The UOR performance of the CoS_2/CeO_2 catalyst was evaluated in a solution containing 1.0 M KOH and 0.5 M urea in this work. The CoS_2/CeO_2 catalyst demonstrates optimal UOR activity and superior UOR kinetics (Fig. S14a, S14b, and S14c, ESI†), as evidenced by ultralow potentials of 1.25 and 1.36 V at 10 and 100 mA·cm⁻², respectively. Meanwhile, the HER activity of the CoS_2/CeO_2 catalyst was measured in a 1.0 M KOH solution. The HER overpotential for CoS_2/CeO_2 catalyst is 97 mV at 10 mA·cm⁻², which is lower than that of CoS_2 (122 mV) and CeO_2 (198 mV) (Fig. S14e, ESI†). Moreover, the CoS_2/CeO_2 catalyst required only 1.44 V potential in urea-assisted water electrolysis compared to water splitting (Fig. S14f, ESI†), indicating that the substitution of UOR for anode reaction significantly enhances the efficiency of water splitting.
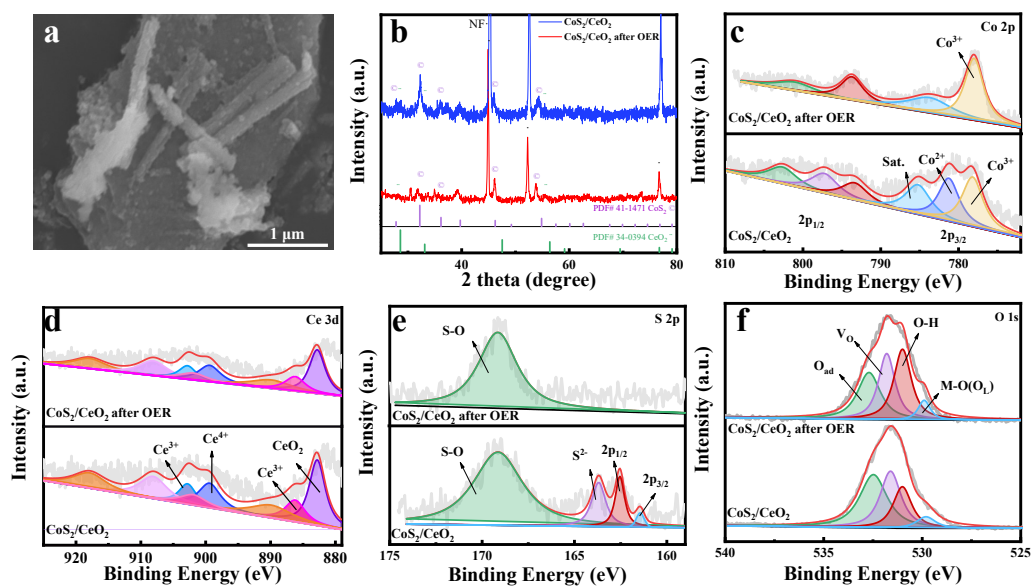
Fig. S16 (a) SEM image, (b) XRD patterns of CoS_2/CeO_2 after OER. XPS spectrum of CoS_2/CeO_2 catalyst before and after OER: (c) Co 2p, (d) Ce $3d_{5/2}$, (e) S 2p, (f) O 1s.

The SEM image (in Fig. S16a) reveals that the rod-like morphology of the CoS_2/CeO_2 catalyst remains largely unchanged after OER. In the XRD patterns (Fig. S16b), it is observed that no new diffraction peak is generated, indicating that the structure is intact after OER. The XPS spectrum after the OER process are presented in Fig. S16c-f. In Fig. S16c, the Co 2p XPS spectrum exhibits peaks at 793.8 and 778.0 eV, which correspond to the characteristic peaks of Co^{3+} ($2p_{1/2}$ and $2p_{3/2}$). Notably, there is a significant increase in the content of Co^{3+} after the OER process. The presence of Ce^{3+} and Ce^{4+} can also be identified in the spectrum of Ce $3d_{5/2}$ (Fig. S16d). The S 2p XPS spectrum (Fig. S16e) reveals the presence of only the peak corresponding to the S-O bond, while the intensity of other peaks is significantly diminished compared to pre-reaction levels. This observation suggests that surface reconstruction of the catalyst took place during the OER process. In the XPS spectrum of O 1s (Fig. S16f), the presence of lattice oxygen (O_L, 529.8 eV), hydroxyl oxygen (-OH, 531.0 eV), oxygen vacancy (V_O, 531.8 eV) and adsorbed oxygen (O_a, 532.7 eV) can be observed after OER with a significant increase in the content of hydroxyl oxygen. [8]
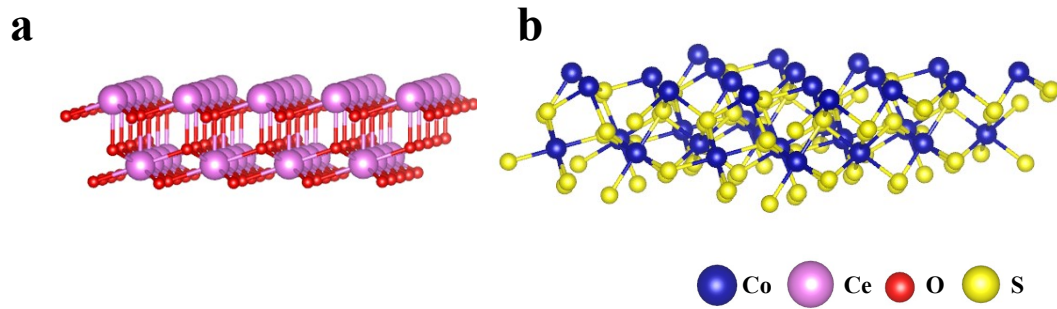
Fig. S17 The atomic models of (a) CeO_2, (b) CoS_2.

a

b
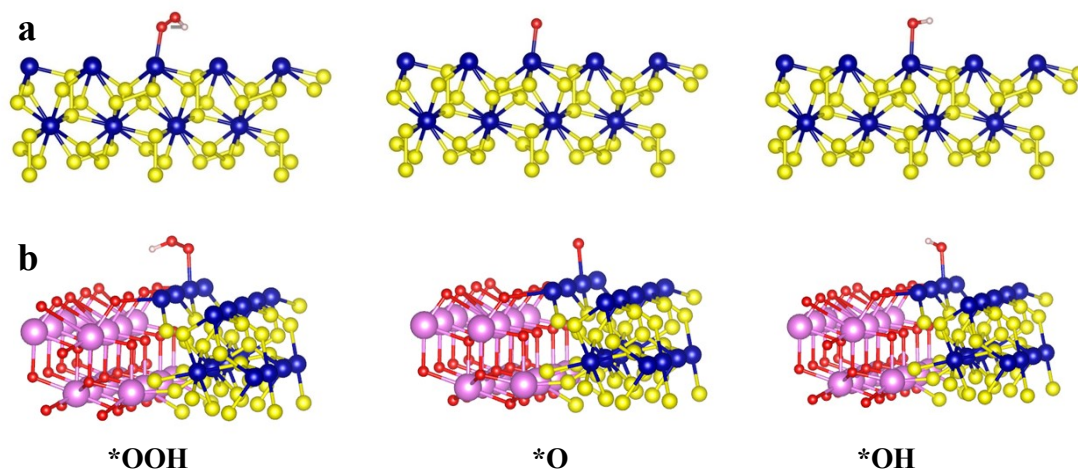
*OOH	*O	*OH

Fig. S18 The intermediate state (*OOH, *O, *OH) of the OER process is constructed on the structure of (a) CoS_2, and (b) CoS_2/CeO_2.
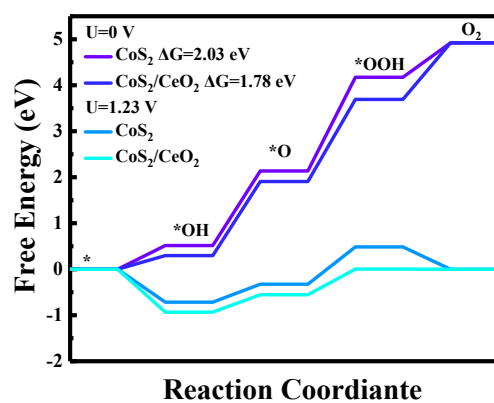
Fig. S19 OER Gibbs free energy distribution of CoS_2 and CoS_2/CeO_2 catalysts at 0 V and 1.23 V.
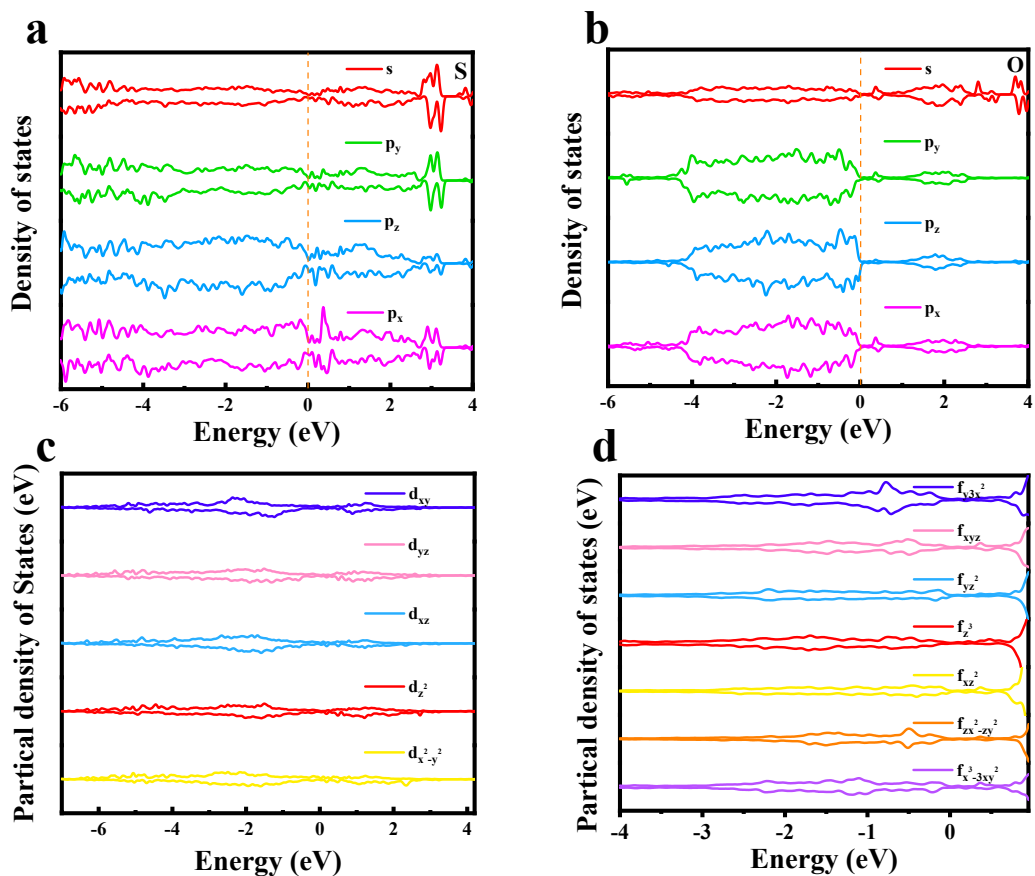
Fig. S20 The PDOS of (a) degenerate S-s,p states, (b) degenerate O-s,p states, (c) degenerate Co-d states and (d) degenerate Ce-f states for CoS_2/CeO_2.
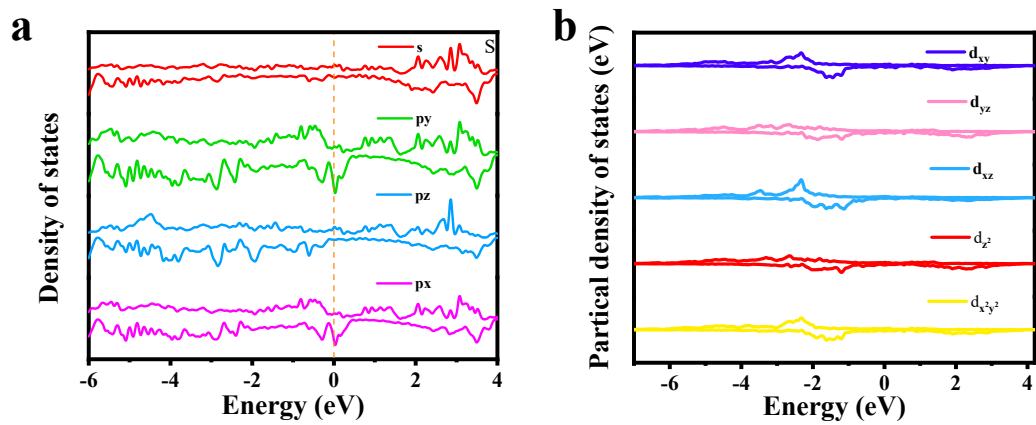
Fig. S21 The PDOS of (a) degenerate S-s,p states,(b) degenerate Co-d states for CoS_2.

Table S1. The surface elements content from XPS.

The carbon element located in 284.79 eV is used for calibration.

| Name	Peak BE (eV)	Height CPS	FWHM (eV)	Area (P) CPS (eV)	Atomic %
Co 2p	779.1	846.86	3.4	11817.48	7.14
Ce 3d	881.79	653.46	0.88	10500.57	1.98
C 1s	284.79	4342.51	1.87	9832.66	-
O 1s	531.73	6025.89	2.55	17385.86	60.25
S 2p	162.22	3157.08	0.72	6332.67	30.63

Table S2. Comparison of OER catalysts performance in this work and recently reported in alkaline medium.

Catalyst	Electrolyte	Substrate	Overpotential (mV)	Reference
CoS_2/CeO_2	1.0 M KOH	Nickel Foam	142	This work
$Ce-m-Ni(OH)_2@NiSe_2$	1.0 M KOH	Nickel Foam	158	Adv. Energy Mater., 2021,11, 2101266
Ce-doped FeNi LDH CFN@VSB-5	1.0 M KOH	Nickel Foam	185	ACS Appl. Energy Mater., 2021, 4, 12836-12847
Ni-Co-Fe-P	1.0 M KOH	Nickel Foam	187	Appl. Catal. B: Environ., 2022, 310, 121353
N, Ce-co-doped CoS_2	1.0 M KOH	Nickel Foam	190	J. Mater. Chem. A, 2020, 8, 22694-22702
$Fe-Co_3O_4$ HNs	1.0 M KOH	Nickel Foam	204	Nano Energy, 2018, 54, 238-250
$N-CoS_2$	1.0 M KOH	Graphene	205	Appl. Catal. B: Environ., 2020, 268, 118449
$CoMnP/Ni_2P$	1.0 M KOH	Nickel Foam	209	J. Mater. Chem. A, 2021, 9, 22129-22139
CoVFeN	1.0 M KOH	Nickel Foam	212	Adv. Energy Mater., 2020, 10, 2002464
$CeO_2@Co_2N$	1.0 M KOH	Nickel Foam	219	Adv. Mater. Interfaces, 2021, 8, 2100041
$CoNiMoO_4-21/CuO_x$	1.0 M KOH	Copper Foam	221	Adv. Energy Mater.,2021, 11, 2102361
Fe–Co MOF	1.0 M KOH	Nickel Foam	224	J. Mater. Chem. A, 2021, 9, 13271-13278
FeCoP	1.0 M KOH	Nickel Foam	227	J. Mater. Chem. A, 2021, 9, 24677-24685
$Cu@CeO_2@NFC-0.25$	1.0 M KOH	Copper Foam	230	Adv. Funct. Mater., 2020, 30, 1908367
$CoNi/CoFe_2O_4$	1.0 M KOH	Nickel Foam	230	J. Mater. Chem. A, 2018, 6, 19221-19230
$Ce-CoS_2$	1.0 M KOH	Titanium Plate	233	J. Mater. Chem. A, 2019, 7, 17775-17781
Co_4N-CeO_2	1.0 M KOH	Graphite Plate	239	Adv. Funct. Mater., 2020, 30, 1910596
$CoS_2@NGC$	1.0 M KOH	Nickel Foam	243	J. Mater. Chem. A, 2020, 8, 6795-6803
NiYCe-MOF	1.0 M KOH	Nickel Foam	245	Nano Lett., 2022, 22, 7238-7245
$S_{4.06}-NiCoVO_x$	1.0 M KOH	Nickel Foam	248	Nanoscale, 2021, 13, 17022-17027
Er-doped CoP	1.0 M KOH	Carbon Cloth	256	J. Mater. Chem. A, 2019, 7, 5769-5778
S-CoTe	1.0 M KOH	Carbon Cloth	257	Small, 2021, 17, 2102027
$(Ni_2Co_1)_{0.925}Fe_{0.075}-MOF$	1.0 M KOH	Nickel Foam	257	Adv. Mater.,2019, 31, 1901139

Co/Ni (BDC)$_2$TED	1.0 M KOH	Copper Foil	260	J. Mater. Chem. A, 2019, 7, 18519-18528
CeO$_2$-NiCoP$_x$	1.0 M KOH	Nickel-cobalt Foam	260	Appl. Catal. B: Environ., 2022, 316, 121678
Co-MoS$_2$/BCCF-21	1.0 M KOH	Pellicles	260	Adv. Mater., 2018, 30, 1801450
Co$_{1-x}$S/Co (OH)F	1.0 M KOH	Carbon Cloth	269	ACS Nano, 2022, 16, 15460-15470
CeO$_x$/NiCo$_2$S$_4$	1.0 M KOH	Carbon Cloth	270	ACS Appl. Mater. Interfaces., 2019, 11, 39841-39847
Fe-doped CoS$_2$	1.0 M KOH	Carbon Cloth	304	Chem. Commun., 2019, 55, 2469-2472
CoS$_2$/Cu$_2$S	1.0 M KOH	Nickel Foam	348	Appl. Catal. B: Environ.,2022, 303, 120849

Reference

1 G. Kresse, J. Furthmüller, Comput. Mater. Sci., 1996, 6, 15-50.

2 G. Kresse, J. Furthmüller, Phys. Rev. B, 1996, 54, 11169-11186.

3 J. P. Perdew, K. Burke, M. Ernzerhof, Phys. Rev. Lett., 1996, 77, 3865-3868.

4 Fei Z, Cococcioni M, Marianetti C A, et al, Phys. Rev. B, 2004, 70, 235121.

5 G. Kresse, D. Joubert, Phys. Rev. B, 1999, 59, 1758-1775.

6 P. E Blöchl, Phys. Rev. B, 1994, 50, 17953-17979.

7 V. Wang, N. Xu, J.C. Liu, et al, Comp. Phys. Commun., 2021, 267, 108033.

8 Y. Chen, J. Wang, Z. Yu, et al, Appl. Catal. B: Environ., 2022, 307, 121151.